Full Title: Clinicopathologic features of a feline SARS-CoV-2 infection model parallel acute COVID-19 in humans

Short Title: SARS-CoV-2-induced acute respiratory distress syndrome in domestic cats: a model to study COVID-19

Authors: Jennifer M. Rudd[1], Miruthula Tamil Selvan[1], Shannon Cowan[1], Yun-Fan Kao[1], Cecily C. Midkiff[2], Jerry W. Ritchey[1], Craig A. Miller[1*]

Affiliations:

[1] Department of Veterinary Pathobiology, College of Veterinary Medicine, Oklahoma State University; Stillwater, OK, USA

[2] Division of Comparative Pathology, National Primate Research Center, Tulane University; Covington, LA, USA

* Corresponding author. Email: craig.miller@okstate.edu (CAM)

Keywords: COVID-19, SARS-CoV-2, Domestic Cats, Feline, Animal Model, ARDS, Pathology

Abstract: The emergence and ensuing dominance of COVID-19 on the world stage has emphasized the urgency of efficient animal models for the development of therapeutics and assessment of immune responses to SARS-CoV-2 infection. Shortcomings of current animal models for SARS-CoV-2 include limited lower respiratory disease, divergence from clinical COVID-19 disease, and requirements for host genetic modifications to permit infection. This study validates a feline model for SARS-CoV-2 infection that results in clinical disease and histopathologic lesions consistent with severe COVID-19 in humans. Intra-tracheal inoculation of concentrated SARS-CoV-2 caused infected cats to develop clinical disease consistent with that observed in the early exudative phase of COVID-19. A novel clinical scoring system for feline respiratory disease was developed and utilized, documenting a significant degree of lethargy, fever, dyspnea, and dry cough in infected cats. In addition, histopathologic pulmonary lesions such as diffuse alveolar damage, hyaline membrane formation, fibrin deposition, and proteinaceous exudates were observed due to SARS-CoV-2 infection, imitating lesions identified in people hospitalized with ARDS from COVID-19. A significant correlation exists between the degree of clinical disease identified in infected cats and pulmonary lesions. Viral loads and ACE2 expression were quantified in nasal turbinates, distal trachea, lung, and various other organs. Natural ACE2 expression, paired with clinicopathologic correlates between this feline model and human COVID-19, encourage use of this model for future translational studies.

Author Summary: Identifying an ideal animal model to study COVID-19 has been difficult, and current models come with challenges that restrict their potential in translational studies. Few lab animals naturally express the receptors necessary for viral infection (ACE2), and many fail to manifest clinical signs or pathology similar to that seen in humans. Other models (non-human primates, mink) are ideal for disease and transmission studies, but are restricted by cost,

husbandry challenges, and scarce availability. Alternatively, cats naturally express ACE2 receptors, are naturally infected with SARS-CoV-2 and can transmit virus from cat-to-cat. Prior to this study, cats infected by oral/nasal routes have not displayed significant clinical disease or lung pathology. However, we demonstrate that direct inoculation of concentrated SARS-CoV-2 virus in the trachea of cats induces analogous clinical and pathologic features to hospitalized patients with acute COVID-19. Our results show that infected cats exhibit significant clinical signs during experimental infection (coughing, increased respiratory effort, lethargy, and fever) and exhibit extensive lung lesions that mimic severe COVID-19 pathology such as diffuse alveolar damage and hyaline membrane formation – highlighting the immeasurable potential for this feline model to address translational approaches for COVID-19 and to better understand the role of cats in transmission and disease.

INTRODUCTION

Since the emergence of severe acute respiratory syndrome coronavirus-2 (SARS-CoV-2) in late 2019, Coronavirus Disease 2019 (COVID-19) has swept across the globe resulting in nearly 3 million deaths worldwide as of March 2021 (1). Although a wide range of clinical symptoms are reported, mortality of COVID-19 patients is closely correlated with progression of viral infection to severe lung disease (pneumonia) and respiratory failure due to acute respiratory distress syndrome (ARDS), which is further complicated by immune cell dyscrasias and hyperinflammation (cytokine storm) in critically ill patients (2-4). Features of pulmonary pathology that are hallmarks of severe COVID-19 (i.e., diffuse alveolar damage with hyaline membrane formation, type II pneumocyte hyperplasia, vascular thrombi, fibrin and serous

63 exudation) have been difficult to reproduce in animal models, making it impossible to
64 completely understand the pathophysiology of disease and to test efficacy of new therapeutics
65 and vaccines (5, 6). Identification of a translational animal model that parallels clinical and
66 pathologic features of disease in addition to route of infection, replication, and transmission
67 kinetics is of paramount importance.

68 SARS-CoV-2 viral infection and replication within a host requires the presence and
69 distribution of angiotensin-converting enzyme 2 (ACE2) receptors similar to humans (7). Natural
70 SARS-CoV-2 infections in animals are documented to occur in a diverse range of species,
71 including domestic and exotic cats, dogs, mink, and Golden Syrian hamsters (8-11), and this
72 diverse host range is largely due to natural expression of ACE2 receptors and host tropism of this
73 receptor with the S protein of SARS-CoV-2 (12, 13). Due to the natural availability of ACE2
74 receptors and confirmed host susceptibility and transmission (10, 14-17), domestic cats offer an
75 exciting advantage as experimental models for SARS-CoV-2 infection (18, 19). Comorbidities
76 that exacerbate COVID-19 disease, such as hypertension, diabetes, renal disease, and obesity, are
77 readily adapted to feline models (20-25). Furthermore, establishing a SARS-CoV-2 infected
78 feline model is prudent to better understand zoonotic transmission potential from domestic cats
79 back to people in close contact.

80 Previous studies have successfully infected cats with SARS-CoV-2 via intra-nasal (1-
81 3.05×10^5 PFU) and/or intra-oral routes (5×10^5 $TCID_{50}$/ml) and have confirmed cat-to-cat
82 transmission through both respiratory droplets and aerosolization (16, 26-28). However, these
83 studies failed to produce clinical signs in infected cats, and evidence of lower respiratory
84 pathology mirroring severe COVID-19 in humans was not observed (16, 26-28), potentially due
85 to concentration of the viral inoculum and/or inoculation route. Interestingly, pulmonary disease

86 with diffuse alveolar damage was previously documented in cats intra-tracheally infected with
87 $1x10^6$ $TCID_{50}$ SARS-CoV-1, which also resulted in efficient transmission of virus to uninfected
88 animals (29, 30).

89 Based on outcomes of these former studies, we hypothesized that inoculation with a
90 higher concentration of SARS-CoV-2 via the intra-tracheal route would result in pulmonary
91 pathology and clinical disease in domestic cats similar to COVID-19 in human patients. The
92 experiments reported in this study provide the first feline model of SARS-CoV-2 infection with
93 significant lower respiratory disease that displays features of diffuse alveolar damage seen in the
94 early exudative phase of human COVID-19. In addition, SARS-CoV-2 infected cats exhibited
95 clinical signs of lower respiratory disease characterized by increased respiratory effort and
96 coughing in addition to signs of systemic involvement such as pyrexia and lethargy. While the
97 role of cats in zoonotic transmission is still under investigation, the applicability of a clinically
98 significant SARS-CoV-2 feline model with pathological lesions that mirror severe COVID-19 is
99 of high impact for future studies.

100

101 **RESULTS**

102 **SARS-CoV-2 infected cats exhibit clinical signs of lower respiratory disease**

103 In order to clinically assess the feline model in Animal Biosafety Level-3 conditions, a
104 novel clinical scoring system for feline respiratory disease was developed by integrating features
105 of previously utilized systems (31-33) (Table 1). Each cat was assigned a score from 0 to 2 for
106 each of the following categories: body weight loss, activity levels, behavioral changes, body

107 temperature, respiratory effort, ocular or nasal discharge, and coughing. Scores were then
108 summated to assign an overall clinical score for each day.

109 SARS-CoV-2-infected cats exhibited a significant increase in clinical disease scores
110 starting on 4 days post-inoculation (dpi) and then on 5, 6, and 8 dpi when compared to sham-
111 inoculated controls (Fig 1A). Clinical disease peaked on 4 dpi and continued through the study
112 endpoint at day 8. The most prominent clinical signs noted were lethargy and increased
113 respiratory effort, which were observed in 100% (12/12) of SARS-COV-2-infected cats during
114 this study. Both lethargy and respiratory effort increase significantly between 3 and 4 dpi
115 (p=0.0027; p=0.0027) and remained elevated with significantly higher scores through 8 dpi when
116 compared with day 0 (Fig 1B). Coughing was noted in 4 of 12 infected cats with peak clinical
117 signs occurring at 4 dpi. Pyrexia (temperature > 39.2°C) was documented in 8 of 12 SARS-CoV-
118 2 infected cats over the course of the study, while 7 infected cats displayed altered behavior
119 (reduced interest in food or attention) and 5 had measurable weight loss. No cats had ocular or
120 nasal discharge (S1 Table). Sham-inoculated cats did not exhibit clinical signs except for one cat
121 with mild weight loss on day 4.

122

	0 (Healthy)	1	2
Body Weight	No weight loss	0 to 5% weight loss	> 5% weight loss
Temperature	37.2 to 39.1° C	39.2 to 39.7° C	> 39.7° C
Respiratory Effort	Normal resting respiratory rate and normal effort	Mild tachypnea, but no overt increase in effort	Marked increase in both respiratory rate and effort; dyspnea
Activity	Normal	Reduced activity when disturbed* (lethargy)	Little to no activity disturbed*; reduced activity stimulated**
Behavior	Normal	Reduced interest in food and/or attention	Anorexia and lack of interest
Ocular/Nasal Discharge	None	Mild discharge noted	Discharge evident from both nasal and ocular regions
Coughing/ Wheezing	None	Mild wheezing, but no coughing	Coughing and/or marked wheezing

123 ***Disturbed**: observer in the room, but kennel unopened
124 ****Stimulated**: kennel open
125 **Table 1. Clinical Scoring System for Feline Respiratory Disease**. A scoring system was
126 designed to assess clinical lower respiratory and systemic disease in the feline model. Each cat
127 was scored daily at the same time point (morning) by a small animal clinician (JMR). Cats were
128 assigned a score from 0 to 2 for each clinical parameter: body weight, temperature, respiratory
129 effort, activity, behavior, ocular/nasal discharge, coughing/wheezing. The parameter scores were
130 summed to assign an overall score per cat per day. Potential scores can range from 0 (healthy
131 with no signs of disease) to 14 on any given day. Resting respiratory rate was considered normal
132 if <36 breaths per minute. Marked increases in rate were >50 breaths per minute at rest.
133 Temperatures were obtained via thermal microchips, and body weights were obtained last to
134 limit stress affecting clinical scoring.

135 **Feline SARS-CoV-2 infection pathology mirrors acute COVID-19**

136 Complete post-mortem evaluation was performed for all sham-inoculated control animals
137 (n=6) and SARS-CoV-2-infected cats euthanized on day 4 (n=6) and day 8 (n=6) post-
138 inoculation. Necropsy tissues from SARS-CoV-2-infected cats (including lung, trachea, nasal
139 turbinates, and tracheobronchial lymph node (TBLN)) were grossly examined and compared to
140 those from sham-inoculated cats (Fig 2 A-C). At 4 dpi, the lungs of SARS-CoV-2-infected cats
141 were grossly heavy and wet, with large multifocal to coalescing regions of dark red consolidation
142 that exuded a moderate amount of edema upon cut section (Fig 2 B). Gross lung lesions were
143 similar at 8 dpi in SARS-CoV-2-infected cats, although the degree of pulmonary edema was
144 moderately more pronounced (Fig 2 C). The TBLN of all SARS-CoV-2-infected cats were
145 diffusely enlarged 4-5 times normal at both 4 dpi (n=6) and 8 dpi (n=6).

146 Microscopic evaluation of selected necropsy tissues (lung, trachea, nasal turbinates, TBLN,
147 and kidney) was performed for all study animals. Tissue sections from all sham-inoculated
148 animals (n=6) were histologically unremarkable (Fig 2 D and S2 Table). In contrast,
149 histopathologic features of feline SARS-CoV-2 infection exhibited striking similarities to
150 documented pathologic features of the acute (exudative) and organizing phases of human
151 COVID-19 (34-37). At 4 dpi, 100% (6/6) of SARS-COV-2 -infected cats exhibited a significant
152 degree of lung pathology (interaction, $p<0.0001$) and prominent histologic features consistent
153 with diffuse alveolar damage (DAD) (Fig 2 E-F). Pulmonary edema (5/6 cats), multifocal
154 alveolar damage and necrosis (5/6 cats), perivascular lymphocytic and neutrophilic infiltrates
155 (6/6 cats), and increased intra-alveolar macrophages (5/6 cats) were significantly elevated in
156 SARS-CoV-2-infected cats at 4 dpi (Supporting Information). These changes were occasionally

157 accompanied by multifocal areas of hyaline membrane formation (3/6 cats), mild to moderate
158 amounts of intra-alveolar fibrin (2/6 cats), type II pneumocyte hyperplasia (2/6 cats), and intra-
159 alveolar syncytial cells (2/6 cats). One SARS-CoV-2 infected cat exhibited severe inflammation
160 in the distal trachea at 4 dpi characterized by multifocal areas of submucosal necrosis and
161 fibrinoid vasculitis with multifocal areas of mucosal ulceration and diphtheritic membrane
162 formation (Fig 2 G).

163 Similar histologic features of DAD were also observed in the lungs of SARS-CoV-2-infected
164 cats at 8 dpi, however, the overall pattern of lung injury appeared exhibited more prominent
165 features of vascular injury compared to day 4 (Fig 2 H). A significant degree of pulmonary
166 edema/exudate, perivascular inflammatory infiltration, and alveolar histiocytosis was present in
167 100% of SARS-CoV-2 animals (6/6 cats) at 8 dpi (Supporting Information). Alveolar damage
168 and necrosis (4/6 cats) and intra-alveolar fibrin (3/6 cats) were also prominent features at this
169 time point. Moreover, histologic evidence of fibrinoid vasculitis (2/6 cats) and vascular
170 thrombosis (2/6 cats) was also observed at 8 dpi, in addition to occasional viral syncytia (1/6
171 cats) (Fig 2H). In 2 of these cats, the tracheal submucosa was multifocally expanded and effaced
172 by moderate to severe lymphoplasmacytic, histiocytic, and neutrophilic inflammation with
173 necrosis (Fig 2 I).

174 A positive linear correlation exists between peak clinical scores and histopathology scores of
175 the lungs in SARS-CoV-2 infected cats (p=0.0002; R^2=0.5884) indicating that severe clinical
176 signs of disease correlate with pulmonary pathology (S1 Fig). Mild, multifocal lymphofollicular
177 inflammation was observed in the nasal turbinates of all SARS-CoV-2-infected cats (6/6) at 4 dpi
178 and in 4/6 cats at 8 dpi, with variable neutrophilic infiltration (Supporting Information). All

179 SARS-CoV-2-infected animals (12/12) exhibited mildly increased lymphoid hyperplasia in
180 TBLN at 4 and 8 dpi characterized by increased medullary cords and extranodal proliferations
181 (Supporting Information), but overall changes were not statistically significant. No significant
182 histopathologic findings were observed in renal tissues at either time point. Fluorescent
183 immunohistochemistry was performed to detect SARS-CoV-2 positive cells in lung and TBLN
184 of 2 SARS-CoV-2 infected cats (n=1 at 4 dpi, n=1 at 8 dpi). At both time points, low numbers of
185 mononuclear cells positive for SARS-CoV-2 nucleoprotein were detected within the medulla of
186 the TBLN, however, no positive cells were observed in lungs of these animals. (Fig 3).

187 **ACE2 expression and viral RNA in feline tissues during SARS-CoV-2 infection**

188 SARS-CoV-2 viral RNA and fACE2 RNA expression was quantified in the nasal
189 turbinates, TBLN, distal trachea, kidneys and lungs of all SARS-CoV-2-infected cats (n=12) and
190 sham-inoculated controls (n=6) using ddPCR (Fig 4 and S3 Table). Viral RNA was detected in
191 100% of tissues collected on 4 dpi from SARS-CoV-2-infected cats (Fig 4 A). At 8 dpi, viral
192 RNA was also detectable in the lung, TBLN, and kidney tissues of all (6/6) infected cats, and in
193 5/6 cats in the nasal turbinates and 5/6 cats in the distal trachea. No SARS-CoV-2 viral RNA was
194 detected in tissues collected from sham-inoculated cats at either time point (S3 Table). SARS-
195 CoV-2 viral RNA copies were elevated in the TBLN at 8 dpi compared with day 4 samples,
196 although this trend was not significant (p=0.0567). In contrast, SARS-CoV-2 viral load in lung
197 samples was significantly lower at 8 dpi than at 4 dpi (p=0.0007) (Figure 4 A). A positive linear
198 correlation was observed between SARS-CoV-2 RNA in the lung and pulmonary histopathology

199 scores of SARS-CoV-2 infected cats (p=0.0183; R^2=0. 3012) (S1 Fig). SARS-CoV-2 RNA was
200 not reliably detected in nasal swabs or plasma of infected cats at either time point.
201 In sham-inoculated cats, Kruskal Wallis test revealed that fACE2 RNA in the nasal
202 turbinates was significantly higher than in the lung (p=0.0093) and TBLN (p=0.0049). fACE2
203 RNA was also higher in the kidney when compared to lung (p=0.0003), trachea (p=0.0034), and
204 TBLN (p=0.0001). These findings were similar in SARS-CoV-2-infected animals at 4 and 8 dpi,
205 with fACE2 RNA levels being significantly higher in the nasal turbinates and kidney versus
206 other tissues (p<0.05) (S4 Table). Overall, fACE2 RNA in the kidney was significantly increased
207 in SARS-CoV-2 infected cats on 4 dpi when compared to both sham-inoculated controls, as well
208 as SARS-CoV-2 infected cats on 8 dpi (ANOVA, p<0.0001) (Figure 4 B). No other significant
209 changes in ACE2 RNA were observed over time.
210

211 **DISCUSSION**

212 The potential of this feline model for future evaluation of COVID-19 is extensive.
213 Challenges with earlier feline models of SARS-CoV-2 infection included a lack of clinical
214 disease and/or pathology of the lower respiratory tract that resembles lesions seen in patients
215 with COVID-19. The differences in clinical presentation between previous feline models and the
216 model described here are likely attributed to modifications in routes and concentration of
217 inoculation. In this study, SARS-CoV-2 was inoculated through an intra-tracheal route and at a
218 higher concentration than previously reported (16, 26, 27). Route of inoculation is an important
219 consideration when establishing an animal model for disease, and previous studies have

220 exhibited marked differences in primary disease severity and distribution based on route of
221 inoculation (38, 39).

222 While previous feline models offer value for study of asymptomatic infections, viral
223 shedding, and transmission of SARS-CoV-2, cats infected through an intra-tracheal route exhibit
224 clinical disease that aligns with that seen in early phases of acute COVID-19. Clinical
225 assessment of infectious lower respiratory disease in a cat can be challenging, and it is not
226 uncommon for cats with confirmed histologic infectious pneumonia to have limited clinical
227 respiratory signs (40). Therefore, the clinical signs of respiratory disease induced in this model
228 are highly significant. A novel clinical scoring system was designed that could be applied in the
229 Animal Biosafety Level-3 facility to carefully assess for clinical disease. Interestingly, the
230 disease noted in the SARS-CoV-2 infected cats was similar to that described in hospitalized
231 patients with COVID-19. Clinical disease of hospitalized human COVID-19 patients is
232 characterized by fever (70-90%), dry cough (60-86%), shortness of breath (53-80%), and fatigue
233 (38%) (41) while predominant clinical sings in SARS-CoV-2 infected cats consisted of fever,
234 cough, lethargy and increased respiratory effort, with lethargy and increased respiratory effort
235 being the most notable clinical signs (Fig 1).

236 In addition to clinical signs of lower respiratory and systemic disease, SARS-CoV-2
237 infected cats also exhibited conspicuous pulmonary lesions of diffuse alveolar damage (DAD) by
238 4 dpi, and additional evidence of vascular damage by 8 dpi (Fig 2). Specific histopathological
239 lesions align closely with those reported in human COVID-19 patients (34-36, 42-44), including
240 DAD resulting in hyaline membrane formation, type II pneumocyte hyperplasia, occasional
241 intra-alveolar syncytial cells, and the development of fibrinous exudate and vascular thrombi. To

242 the author's knowledge, this is the first report of hyaline membrane formation and type II
243 pneumocyte hyperplasia in feline SARS-CoV-2 infection. Peak clinical disease scores positively
244 correlated with severity of histologic lesions in the lungs (S1 Fig), which further support that cats
245 with marked pulmonary histologic damage also had more severe clinical signs of disease.

246 Surprisingly, intra-tracheal inoculation of SARS-CoV-2 did not produce high viral RNA
247 loads in the lungs as compared with other studies in which the inoculate was delivered via the
248 intranasal route (26). However, despite by-passing the upper airway, virus was still detected in
249 the nasal turbinates by 4 and 8 dpi, suggesting the virus may utilize the mucociliary escalator to
250 travel up the respiratory tree and establish infection intra-nasally even without intra-nasal
251 inoculation. Although seemingly lower quantities of SARS-CoV-2 RNA were recovered from
252 lungs of intra-tracheally inoculated cats, the damage to lung tissues was highly evident,
253 indicating that extensive pulmonary damage will occur even without high levels of viral
254 replication within the pulmonary tissue at 4 and 8 dpi. Viral migration from lung to the TBLN
255 occurred quickly (by 4 dpi) and this TBLN involvement is a novel finding to the feline model of
256 SARS-CoV-2, including detection of viral antigen within the TBLN via fluorescent
257 immunohistochemistry.

258 Similar to humans, fACE2 RNA expression varied by tissue location, but were relatively
259 low in the lungs of both infected and uninfected cats. It is important to note that RNA
260 measurements indicate an upregulation or downregulation of production of proteins, but do not
261 necessarily indicate an absolute number of receptors available. However, it is possible that
262 inefficient replication and rapid clearance of SARS-CoV-2 in the lungs is related to lower
263 expression of ACE2 receptors as compared with nasal turbinate ACE2. Histopathology shows

264 that cells regularly expressing ACE2 are damaged in the lung and this viral-induced pulmonary
265 epithelial pathology may contribute further. ACE2 RNA copies in the feline kidney are
266 significantly higher than that of other assessed tissues, and viral infection resulted in a significant
267 upregulation of ACE2 RNA by 4 dpi and then a subsequent reduction by 8 dpi. Hypertension and
268 activation of the renin-angiotensin system may have driven this rise in ACE2 in order to
269 counterbalance system effects on infection, and future studies should include blood pressure
270 evaluation in conjunction with other clinical parameters such as oxygen saturation, chemistry
271 panels, and imaging. Further studies are needed to fully understand the role of ACE2 in SARS-
272 CoV-2 viral replication kinetics and disease.

273 Limitations to this study include sample sizes as well as sampling time points. Further
274 studies are needed to try and better identify peak viral loads in various tissues as well as ACE2
275 expression in order to investigate when viral clearance occurs and when this feline model moves
276 from early exudative disease to more organized, fibrotic disease. A better delineation of these
277 events would add value to the model and its potential for use at other stages of disease. In
278 addition, transmission and viral shedding after intra-tracheal inoculation of SARS-CoV-2 should
279 be evaluated and compared with that of intra-nasal inoculation and spread. Expansion of in depth
280 diagnostics was limited due to animal biosafety level requirements and availability of resources,
281 but future studies will seek to evaluate other clinical parameters, such as oxygen saturation,
282 thoracic imaging and complete blood counts, chemistry panels and urine analysis to better assess
283 damage to other organ systems and further compare with human disease.

284 This feline model of SARS-CoV-2 infection offers an animal model that closely mirrors
285 both clinical disease and pathology identified in hospitalized patients with severe COVID-19,

286 making the model a potential option for future studies addressing novel therapeutics for COVID-
287 19. Therapeutic measures can be thoroughly assessed for improvement in pathology and
288 mitigation of clinical disease in cats before being validated in human trials, and more thorough
289 evaluation of the feline immune response to infection may elucidate other options for COVID-19
290 treatments that could mitigate disease and improve clinical outcomes. The continued emergence
291 of novel variants, circulating globally, ceaselessly contributes to the complexity and duration of
292 this pandemic. This animal model offers an ease of use, which can positively impact further
293 vaccination and control strategies necessary to achieve an end to the rapid spread of COVID-19.
294 This model also offers utility in a One Health approach to the role of companion animals in
295 disease transmission, antigenic drift, and more thorough evaluation of the potential for feline
296 contributions to the spread of SARS-CoV-2.

297

298 **MATERIALS AND METHODS**

299 **Ethics Statement.** This study was approved by the Oklahoma State University Institutional
300 Animal Care and Use Committee; IACUC-20-48, Validation of a naturally occurring animal
301 model for SARS-CoV-2 infection. Oklahoma State University's animal care and use program is
302 licensed by the United States Department of Agriculture (USDA), and accredited by the
303 Association for Assessment and Accreditation of Laboratory Animal Care (AAALAC). In
304 accordance with the approved IACUC protocol, animals were monitored at least once daily for
305 evidence of morbidity and discomfort by trained animal care staff. Prior to experimental
306 procedures, all study animals were anesthetized to minimize animal suffering and distress.
307 Human euthanasia procedures were conducted by phenobarbital overdose in accordance with

308 IACUC protocols and American Veterinary Medical Association (AVMA) Guidelines for the
309 Euthanasia of Animals. Prior to euthanasia, all study animals were anesthetized by intramuscular
310 injection of ketamine (4 mg/kg), dexmedetomidine (0.02 mg/kg), and butorphanol (0.4 mg/kg).
311 No animals died without euthanasia during this study.

312 **Virus.** SARS-CoV-2 virus isolate USA-WA1/2020 was obtained from BEI Resources, passaged
313 up to 6 times in Vero E6 cells in Vero E6 cell growth medium. Virus stock was titrated and
314 quantified on Vero E6 cells using a standard MERS-CoV quantification assay (45). $TCID_{50}$ was
315 calculated using the Reed and Muench method.

316 **Animals.** Eighteen adult (9 males, 9 females, all 9 months-old) specific pathogen free (SPF) cats
317 were obtained from Marshall BioResources (North Rose, NY). Animals intended for SARS-
318 CoV-2 inoculation were housed within Biosafety Level 3 (BSL-3) barrier animal rooms at
319 Oklahoma State University, individually housed and fed dry/wet food with access to water *ad*
320 *libitum*. Animals intended for sham-inoculation were group-housed within the AAALAC
321 International Accredited animal facility at Oklahoma State University. Animals were allowed 30
322 days for acclimation prior to initiation of the study. Temperature-sensing microchips (Bio Medic
323 Data Systems, Seaford, DE) were implanted subcutaneously in the dorsum after 30 days.
324 Baseline weights, body temperatures, clinical evaluation, and nasal swab sampling were obtained
325 prior to inoculation. All animals were in apparent good health at the onset of the study.

326 **Virus Challenge.** Cats were lightly anesthetized with ketamine (4 mg/kg), dexmedetomidine (20
327 µg/kg), and butorphanol (0.4 mg/kg) intramuscularly. Cats were then positioned in ventral
328 recumbency and intubated so that the end of an endotracheal tube is positioned within the distal
329 trachea as described (46). In twelve cats, a 3-cc syringe was used to inoculate 1 mL $9x10^5$ PFU

330 ($1.26x10^6$ $TCID_{50}$) per mL SARS-CoV-2, isolate USA-WA1/2020 in Dulbecco's Modified Eagle
331 Medium (DMEM), followed by 2 mL of air from an empty syringe. The remaining six cats were
332 sham-inoculated using sterile PBS via the same method. Viral inoculum dosage was confirmed
333 through virus back-titration on E6 cells immediately following inoculation.

334 **Sampling.** Blood and nasal swab samples were collected under sedation (described above) from
335 all study animals (n=18) at day 0 to serve as baseline for ddPCR analysis. Blood samples (6 mL)
336 were obtained from all cats via cephalic or medial saphenous venipuncture and processed
337 immediately for viral quantification. Nasal swab samples obtained from the nares of all cats
338 using ultrafine flocked swabs (Puritan) were placed in 2 mL microcentrifuge tubes containing
339 RNAlater solution (Ambio, Austin, TX) and stored at -80°C until processed. At day 4 and day 8
340 post-inoculation, a subset of SARS-CoV-2 infected cats (n=6 per time point) and sham-
341 inoculated control cats (n=3 per time point) were anesthetized for blood and nasal swab
342 collection then humanely euthanized (pentobarbital >80mg/kg) and necropsied to collect tissue
343 samples. Necropsied tissues were processed for histologic examination, immunohistochemistry
344 (IHC), and RNA analysis as described below.

345 **Clinical Observations and Scoring.** Animals were monitored at least once daily for evidence of
346 morbidity and discomfort by a licensed veterinary practitioner. Body weights and temperatures
347 (thermal microchips) were documented daily every morning for the duration of the study. Full
348 clinical scoring included evaluation of body weight, body temperature, activity levels, behavior,
349 respiratory effort, evidence of ocular/nasal discharge, and recognition of coughing or wheezing.
350 Each factor was assigned a score of 0 (normal), 1 (mild-moderate), or 2 (severe) as described in
351 Table 1. Each clinical factor parameter was added to assign an individual animal a summed

352 clinical score every 24 hours for the duration of the study. Cats were observed at rest for
353 respiration rates, activity levels and other notable clinical signs before stimulation.

354 **Histopathology**. Necropsy was performed on six (n=6) SARS-CoV-2-infected cats at 4 dpi and
355 the remaining six (n=6) SARS-CoV-2-infected cats at 8 dpi. Three (n=3) sham-inoculated cats
356 were necropsied at each time point (4 dpi and 8 dpi) to provide control samples. Tissue
357 collection included: lung, tracheobronchial lymph nodes, nasal turbinates, distal trachea, and
358 kidney. Necropsy tissues were halved and then placed into either 1 mL tubes and frozen at -
359 80°C, or into standard tissue cassettes that were then fixed in 10% neutral-buffered formaldehyde
360 for 96 hours prior transferring to 70% ethanol for 72 hours. Tissues were then trimmed and
361 processed for histology. Five µm paraffin sections were collected onto charged slides, and one
362 slide of each tissue was stained with hematoxylin and eosin (H & E) for microscopic evaluation.
363 Necropsy tissues were evaluated for evidence of inflammation and/or aberrations in lymphoid
364 populations as reported in human COVID-19 patients (34-37). Lung tissues were specifically
365 evaluated for the following pathology: alveolar damage (pneumocyte necrosis, hyaline
366 membrane formation,) alveolar fibrin deposition (± organization), serous exudate/edema,
367 perivascular infiltrates, alveolar histiocytes, type II pneumocyte hyperplasia, syncytia,
368 thrombosis, and fibrinoid vasculitis. All tissues were assigned a quantitative histologic score
369 based on previously documented criteria (47, 48): 0 = no apparent pathology/change; 1 =
370 minimal change (minimally increased numbers of inflammatory cells); 2 = mild change (mild
371 inflammatory infiltrates, alveolar damage/necrosis, fibrin deposition and/or exudation); 3 =
372 moderate change (as previously described, but more moderately extensive); 4 = marked changes
373 (as previously described, but with severe inflammation, alveolar damage, hyaline membrane
374 formation, necrosis, exudation, vasculitis and/or thrombosis). All tissues were evaluated and

375 scored by a board-certified veterinary pathologist blinded to study groups to ensure scientific
376 rigor and reproducibility.

377 **Viral RNA Analysis.** Viral RNA analysis was performed on samples from nasal swabs,
378 collected plasma, and tissues. Nasal swabs were immediately broken off into 1.5 mL
379 microcentrifuge tubes containing 200 µL RNAlater Solution (Ambion, Austin, TX) and stored at
380 -20°C. The nasal swabs were vortexed for 15 seconds, then inverted and centrifuged at 1500 rpm
381 for 10 minutes. RNA was extracted from frozen necropsy tissues using a QIAamp Viral RNA
382 Mini Kit (Qiagen, Germantown, MD) and tissue homogenizer. SARS-CoV-2 viral RNA was
383 quantified by droplet digital PCR (ddPCR) as previously described (49). Briefly, ddPCR was
384 performed according to manufacturer's instructions for the 2019-nCoV CDC ddPCR Triplex
385 Probe Assay (Bio-Rad, Hercules, California, USA). PCR reaction mixtures were as follows: 5.5
386 µl One-Step RT-ddPCR Advanced Kit for Probes Supermix (no dUTP's) (Bio-Rad), 2.2 µl
387 reverse transcriptase, 1.1 µl 300 mM Dithiothreitol (DTT), 1.1 µl triplex probe assay (for N1,
388 N2, RPP30 detection), 2.2 µl RNase free water, and 9.9 µl RNA template in a final volume of 22
389 µl per sample. Duplicate 20 µl samples were partitioned using a QX200 droplet generator (Bio-
390 Rad, Hercules, California, USA) and then transferred to a 96-well plate and sealed. Samples
391 were processed in a C1000 touch Thermal Cycler (Bio-Rad) under the following cycling
392 protocol: 50 °C for 60 min for reverse transcription, 95 °C for 10 min for enzyme activation,
393 94°C for 30 s for denaturation and 55 °C for 60 s for annealing/extension for 45 cycles, 98 °C 10
394 min for enzyme deactivation, 4 °C for 30 min for droplet stabilization followed by infinite 4 °C
395 hold. The amplified samples were read in the FAM and HEX channels using the QX200 reader
396 (Bio-Rad). Each experiment was performed with a negative control (no template control, NTC)
397 and a positive control (RNA extracted from SARS-CoV-2 viral stock and diluted 1:12,000). Data

398 were analyzed using QuantaSoft™ v1 AnalysisPro Software (Bio-Rad) and expressed as Log_{10}
399 (copies/mL).

400 **Feline ACE2 Analysis.** Feline angiotensin converting enzyme 2 (fACE2) RNA was quantified
401 by ddPCR using methods similar to the above assay for CoV. RNA was extracted from frozen
402 necropsy tissues as outlined above. cDNA was synthesized as previously published (48). Design
403 of primers and probe targeting fACE2 was performed according to manufacturer's
404 recommendation, namely keeping GC content between 50–60 % for primers and 30–80 % for
405 probes, and melting temperatures between 50–65 ◦C for primers and 3–10 ◦C higher for probes.
406 Oligoes were synthesized by Integrated DNA Technologies (IDT, Coralville, Iowa, USA). The
407 sequences are as follows: Forward: 5′- ACGGAGGCGTAAGGATTT -3′ , Reverse: 5′ -
408 GTGTGGTAGTGGTTGGTATTG -3′ , probe: 5′ - CGGGATCAGAAATCGAAGGAAGAA -
409 3′. BLAST analysis (50) of the primer and probe sequences against the domestic cat (*Felis catus*)
410 genome was performed to ensure no similar sequences could be amplified. ddPCR reactions
411 were prepared by adding 11 µl Supermix for Probes (no dUTP) (Bio-Rad), 1.1 µl of primer/probe
412 mix (final concentration is 500nM for primers and 250 nM for probe) and 8.8 µl of cDNA
413 template containing 110 ng RNA equivalent. Droplets were partitioned and PCR executed as
414 above using the following cycling conditions: 95 °C for 10 min, 95 °C 30 s for denaturation and
415 58.8 °C for 60 s for annealing/extension for 45 cycles, 98 °C 10 min for enzyme deactivation.
416 Droplets were read and analyzed as described above.

417 **Immunohistochemistry**. 5µm sections of formalin-fixed, paraffin-embedded lung were
418 mounted on charged glass slides, baked for one hour at 60°C, and passed through Xylene, graded
419 ethanol, and double distilled water to remove paraffin and rehydrate tissue sections. A

420 microwave was used for heat induced epitope retrieval. Slides were heated in a high pH solution
421 (Vector Labs H-3301), rinsed in hot water and transferred to a heated low pH solution (Vector
422 Labs H-3300) where they were allowed to cool to room temperature. Sections were washed in a
423 solution of phosphate-buffered saline and fish gelatin (PBS-FSG) and transferred to a humidified
424 chamber, for staining at room temperature. Tissues were blocked with 10% normal goat serum
425 (NGS) for 40 minutes, followed by a 60-minute incubation with a guinea pig anti-SARS
426 antibody (BEI NR-10361) diluted 1:1000 in NGS. Slides were washed and transferred to the
427 humidified chamber for a 40-minute incubation with a goat anti-guinea pig secondary antibody
428 (Invitrogen A11073) tagged with Alexa Fluor 488 and diluted 1:1000 in NGS. Following
429 washes, DAPI (4',6-diamidino-2-phenylindole) was used to label the nuclei of each section.
430 Slides were mounted using a homemade anti-quenching mounting media containing Mowiol
431 (Calbiochem#475904) and DABCO (Sigma #D2522) and imaged at 20X with a Zeiss Axio Slide
432 Scanner.

433 **Statistical Analyses.** When applicable, data were expressed as mean ± SEM and statistically
434 analyzed using GraphPad Prism 9.0 software (La Jolla, CA). Kruskal–Wallis test, Pearson
435 correlations, and ANOVA were used to compare differences in clinical score, histopathology,
436 SARS-CoV-2 viral load, and ACE2 RNA among uninfected and SARS-CoV-2-infected
437 individuals, between sample type, for each tissue individually, and between tissues. For all
438 significant results, pair-wise comparisons were made by post-hoc analysis. P-values < 0.05 were
439 considered significant.

440 **Acknowledgments**: The authors would like to thank Girish Patil, Akhilesh Ramachandran, and
441 Sai Narayanan with the Oklahoma Animal Disease Diagnostic Lab for their assistance in viral

442 RNA extraction and technical advisement. We would also like to acknowledge Curtis Andrew
443 for assistance with slide preparation and coordination of immunohistochemistry from the
444 Immunopathology Core Laboratory at Oklahoma State College of Veterinary Medicine.

445

446 **References**

447 1. WHO. World Health Organization Coronavirus (COVID-19) Dashboard: World Health
448 Organization; 2021 [cited 2021. Available from: https://covid19.who.int.
449 2. Wu C, Chen X, Cai Y, Zhou X, Xu S, Huang H, et al. Risk factors associated with acute
450 respiratory distress syndrome and death in patients with coronavirus disease 2019 pneumonia
451 in Wuhan, China. JAMA internal medicine. 2020.
452 3. Chen G, Wu D, Guo W, Cao Y, Huang D, Wang H, et al. Clinical and immunologic features
453 in severe and moderate Coronavirus Disease 2019. The Journal of Clinical Investigation.
454 2020.
455 4. Pedersen SF, Ho Y-C. SARS-CoV-2: a storm is raging. The Journal of Clinical Investigation.
456 2020.
457 5. Kumar S, Yadav PK, Srinivasan R, Perumal N. Selection of animal models for COVID-19
458 research. Virusdisease. 2020;31(4):1-6.
459 6. Gretebeck LM, Subbarao K. Animal models for SARS and MERS coronaviruses. Curr Opin
460 Virol. 2015;13:123-9.
461 7. Hikmet F, Méar L, Edvinsson Å, Micke P, Uhlén M, Lindskog C. The protein expression
462 profile of ACE2 in human tissues. Mol Syst Biol. 2020;16(7):e9610.

463 8. Kiros M, Andualem H, Kiros T, Hailemichael W, Getu S, Geteneh A, et al. COVID-19
464 pandemic: current knowledge about the role of pets and other animals in disease
465 transmission. Virol J. 2020;17(1):143.
466 9. Oreshkova N, Molenaar RJ, Vreman S, Harders F, Oude Munnink BB, Hakze-van der
467 Honing RW, et al. SARS-CoV-2 infection in farmed minks, the Netherlands, April and May
468 2020. Euro Surveill. 2020;25(23).
469 10. Newman A, Smith D, Ghai RR, Wallace RM, Torchetti MK, Loiacono C, et al. First
470 Reported Cases of SARS-CoV-2 Infection in Companion Animals - New York, March-April
471 2020. MMWR Morb Mortal Wkly Rep. 2020;69(23):710-3.
472 11. Molenaar RJ, Vreman S, Hakze-van der Honing RW, Zwart R, de Rond J, Weesendorp E, et
473 al. Clinical and Pathological Findings in SARS-CoV-2 Disease Outbreaks in Farmed Mink
474 (Neovison vison). Vet Pathol. 2020;57(5):653-7.
475 12. Luan J, Lu Y, Jin X, Zhang L. Spike protein recognition of mammalian ACE2 predicts the
476 host range and an optimized ACE2 for SARS-CoV-2 infection. Biochem Biophys Res
477 Commun. 2020;526(1):165-9.
478 13. Liu Y, Hu G, Wang Y, Ren W, Zhao X, Ji F, et al. Functional and genetic analysis of viral
479 receptor ACE2 orthologs reveals a broad potential host range of SARS-CoV-2. Proc Natl
480 Acad Sci U S A. 2021;118(12).
481 14. Hayashi T, Abiko K, Mandai M, Yaegashi N, Konishi I. Highly conserved binding region of
482 ACE2 as a receptor for SARS-CoV-2 between humans and mammals. Vet Q.
483 2020;40(1):243-9.

484 15. McAloose D, Laverack M, Wang L, Killian ML, Caserta LC, Yuan F, et al. From People to
485 Panthera: Natural SARS-CoV-2 Infection in Tigers and Lions at the Bronx Zoo. mBio.
486 2020;11(5).
487 16. Shi J, Wen Z, Zhong G, Yang H, Wang C, Huang B, et al. Susceptibility of ferrets, cats,
488 dogs, and other domesticated animals to SARS-coronavirus 2. Science. 2020.
489 17. Zhang Q, Zhang H, Gao J, Huang K, Yang Y, Hui X, et al. A serological survey of SARS-
490 CoV-2 in cat in Wuhan. Emerg Microbes Infect. 2020;9(1):2013-9.
491 18. Lakdawala SS, Menachery VD. The search for a COVID-19 animal model. Science.
492 2020;368(6494):942-3.
493 19. Hernández M, Abad D, Eiros JM, Rodríguez-Lázaro D. Are Animals a Neglected
494 Transmission Route of SARS-CoV-2? Pathogens. 2020;9(6).
495 20. Van de Velde H, Janssens GP, de Rooster H, Polis I, Peters I, Ducatelle R, et al. The cat as a
496 model for human obesity: insights into depot-specific inflammation associated with feline
497 obesity. Br J Nutr. 2013;110(7):1326-35.
498 21. Nelson RW, Reusch CE. Animal models of disease: classification and etiology of diabetes in
499 dogs and cats. J Endocrinol. 2014;222(3):T1-9.
500 22. Samaha G, Beatty J, Wade CM, Haase B. The Burmese cat as a genetic model of type 2
501 diabetes in humans. Anim Genet. 2019;50(4):319-25.
502 23. Hoenig M. The cat as a model for human obesity and diabetes. J Diabetes Sci Technol.
503 2012;6(3):525-33.
504 24. Wallner M, Eaton DM, Berretta RM, Borghetti G, Wu J, Baker ST, et al. A Feline HFpEF
505 Model with Pulmonary Hypertension and Compromised Pulmonary Function. Sci Rep.
506 2017;7(1):16587.

507 25. Prat V, Rozec B, Gauthier C, Lauzier B. Human heart failure with preserved ejection versus
508 feline cardiomyopathy: what can we learn from both veterinary and human medicine? Heart
509 Fail Rev. 2017;22(6):783-94.
510 26. Gaudreault NN, Trujillo JD, Carossino M, Meekins DA, Morozov I, Madden DW, et al.
511 SARS-CoV-2 infection, disease and transmission in domestic cats. Emerg Microbes Infect.
512 2020;9(1):2322-32.
513 27. Bosco-Lauth AM, Hartwig AE, Porter SM, Gordy PW, Nehring M, Byas AD, et al.
514 Experimental infection of domestic dogs and cats with SARS-CoV-2: Pathogenesis,
515 transmission, and response to reexposure in cats. Proc Natl Acad Sci U S A.
516 2020;117(42):26382-8.
517 28. Gaudreault NN, Carossino M, Morozov I, Trujillo JD, Meekins DA, Madden DW, et al.
518 Experimental re-infected cats do not transmit SARS-CoV-2. Emerg Microbes Infect.
519 2021;10(1):638-50.
520 29. van den Brand JM, Haagmans BL, Leijten L, van Riel D, Martina BE, Osterhaus AD, et al.
521 Pathology of experimental SARS coronavirus infection in cats and ferrets. Vet Pathol.
522 2008;45(4):551-62.
523 30. van den Brand JM, Haagmans BL, van Riel D, Osterhaus AD, Kuiken T. The pathology and
524 pathogenesis of experimental severe acute respiratory syndrome and influenza in animal
525 models. J Comp Pathol. 2014;151(1):83-112.
526 31. Huet O, Ramsey D, Miljavec S, Jenney A, Aubron C, Aprico A, et al. Ensuring animal
527 welfare while meeting scientific aims using a murine pneumonia model of septic shock.
528 Shock. 2013;39(6):488-94.

529 32. Hartmann AD, Helps CR, Lappin MR, Werckenthin C, Hartmann K. Efficacy of
530 pradofloxacin in cats with feline upper respiratory tract disease due to Chlamydophila felis or
531 Mycoplasma infections. J Vet Intern Med. 2008;22(1):44-52.
532 33. Steagall PV, Monteiro BP. Acute pain in cats: Recent advances in clinical assessment. J
533 Feline Med Surg. 2019;21(1):25-34.
534 34. Polak SB, Van Gool IC, Cohen D, Jan H, van Paassen J. A systematic review of pathological
535 findings in COVID-19: a pathophysiological timeline and possible mechanisms of disease
536 progression. Modern Pathology. 2020;33(11):2128-38.
537 35. Tian S, Xiong Y, Liu H, Niu L, Guo J, Liao M, et al. Pathological study of the 2019 novel
538 coronavirus disease (COVID-19) through postmortem core biopsies. Modern Pathology.
539 2020;33(6):1007-14.
540 36. von der Thüsen J, van der Eerden M. Histopathology and genetic susceptibility in COVID-19
541 pneumonia. European journal of clinical investigation. 2020;50(7):e13259.
542 37. Xu Z, Shi L, Wang Y, Zhang J, Huang L, Zhang C, et al. Pathological findings of COVID-19
543 associated with acute respiratory distress syndrome. The Lancet respiratory medicine.
544 2020;8(4):420-2.
545 38. Bodewes R, Kreijtz JH, van Amerongen G, Fouchier RA, Osterhaus AD, Rimmelzwaan GF,
546 et al. Pathogenesis of Influenza A/H5N1 virus infection in ferrets differs between intranasal
547 and intratracheal routes of inoculation. Am J Pathol. 2011;179(1):30-6.
548 39. Rimmelzwaan GF, van Riel D, Baars M, Bestebroer TM, van Amerongen G, Fouchier RA, et
549 al. Influenza A virus (H5N1) infection in cats causes systemic disease with potential novel
550 routes of virus spread within and between hosts. Am J Pathol. 2006;168(1):176-83; quiz 364.

551 40. Macdonald ES, Norris CR, Berghaus RB, Griffey SM. Clinicopathologic and radiographic
552 features and etiologic agents in cats with histologically confirmed infectious pneumonia: 39
553 cases (1991-2000). J Am Vet Med Assoc. 2003;223(8):1142-50.
554 41. Wiersinga WJ, Rhodes A, Cheng AC, Peacock SJ, Prescott HC. Pathophysiology,
555 Transmission, Diagnosis, and Treatment of Coronavirus Disease 2019 (COVID-19): A
556 Review. Jama. 2020;324(8):782-93.
557 42. Xu Z, Shi L, Wang Y, Zhang J, Huang L, Zhang C, et al. Pathological findings of COVID-19
558 associated with acute respiratory distress syndrome. Lancet Respir Med. 2020;8(4):420-2.
559 43. Fox SE, Akmatbekov A, Harbert JL, Li G, Quincy Brown J, Vander Heide RS. Pulmonary
560 and cardiac pathology in African American patients with COVID-19: an autopsy series from
561 New Orleans. Lancet Respir Med. 2020;8(7):681-6.
562 44. Borczuk AC, Salvatore SP, Seshan SV, Patel SS, Bussel JB, Mostyka M, et al. COVID-19
563 pulmonary pathology: a multi-institutional autopsy cohort from Italy and New York City.
564 Mod Pathol. 2020;33(11):2156-68.
565 45. Coleman CM, Frieman MB. Growth and quantification of MERS-CoV infection. Current
566 protocols in microbiology. 2015;37(1):15E. 2.1-E. 2.9.
567 46. Ritchey JW, Levy JK, Bliss SK, Tompkins WA, Tompkins MB. Constitutive expression of
568 types 1 and 2 cytokines by alveolar macrophages from feline immunodeficiency virus-
569 infected cats. Vet Immunol Immunopathol. 2001;79(1-2):83-100.
570 47. Miller C, Bielefeldt-Ohmann H, MacMillan M, Huitron-Resendiz S, Henriksen S, Elder J, et
571 al. Strain-specific viral distribution and neuropathology of feline immunodeficiency virus.
572 Veterinary immunology and immunopathology. 2011;143(3):282-91.

573 48. Miller C, Boegler K, Carver S, MacMillan M, Bielefeldt-Ohmann H, VandeWoude S.
574 Pathogenesis of oral FIV infection. PloS one. 2017;12(9):e0185138.
575 49. Deiana M, Mori A, Piubelli C, Scarso S, Favarato M, Pomari E. Assessment of the direct
576 quantitation of SARS-CoV-2 by droplet digital PCR. Scientific reports. 2020;10(1):1-7.
577 50. O'Driscoll A, Belogrudov V, Carroll J, Kropp K, Walsh P, Ghazal P, et al. HBLAST:
578 Parallelised sequence similarity--A Hadoop MapReducable basic local alignment search tool.
579 J Biomed Inform. 2015;54:58-64.
580 51. Blair RV, Vaccari M, Doyle-Meyers LA, Roy CJ, Russell-Lodrigue K, Fahlberg M, et al.
581 Acute Respiratory Distress in Aged, SARS-CoV-2–Infected African Green Monkeys but Not
582 Rhesus Macaques. The American journal of pathology. 2021;191(2):274-82.
583

584 **Funding:** Research reported in this publication was supported by the National Institute of
585 General Medical Sciences of the National Institutes of Health under Award Number
586 P20GM103648 (CAM). The content is solely the responsibility of the authors and does not
587 necessarily represent the official views of the National Institutes of Health. The funders had no
588 role in study design, data collection and analysis, decision to publish, or preparation of the
589 manuscript. https://www.nih.gov/

590 **Author Contributions:**

591 Conceptualization: CAM, JMR, JWR

592 Methodology: CAM, JMR, JWR, SC, CCM

593 Investigation: CAM, JMR, MTS, SC, JWR, CCM

594 Visualization: CAM, JMR, MTS

595 Funding Acquisition: CAM

596 Writing – original draft: JMR, CAM

597 Writing – review and editing: JWR, CCM, SC, MTS

598

599 **Competing Interests:** The authors have declared that no competing interests exist.

600

601 **Data and materials availability:** All relevant data associated with this study has been deposited
602 in a public repository: 10.6084/m9.figshare.14449773

603 **Figures**

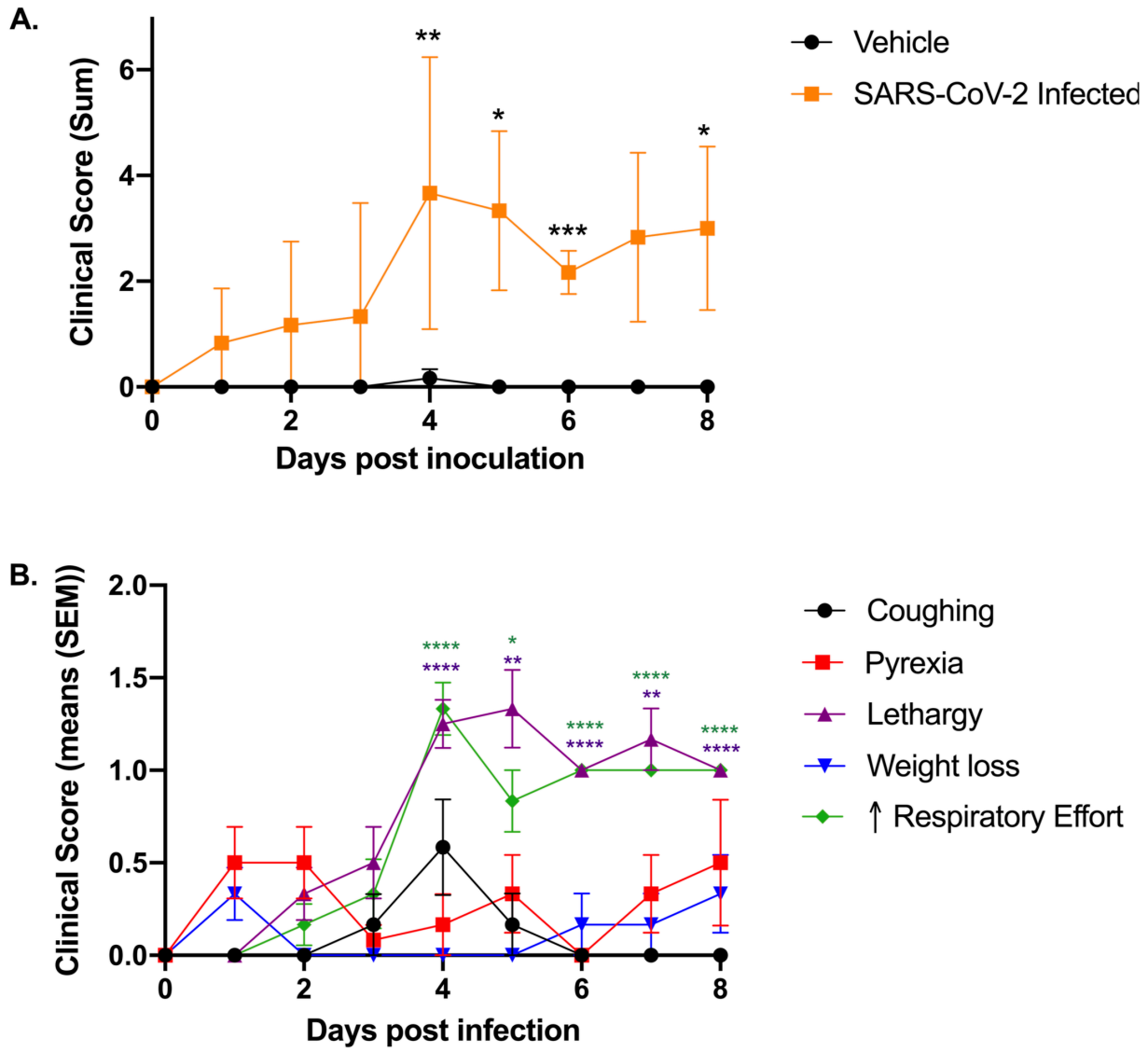

604

605 **Fig 1. Intra-tracheal SARS-CoV-2 inoculation results in clinical disease.** Clinical parameters

606 were assessed using the feline respiratory disease clinical scoring system (see Table 1). **(A)**

607 Clinical parameters summated to provide an overall clinical score per cat per day. Clinical

608 disease severity peaked on 4 dpi and was significantly higher than sham-inoculated cats on 4 dpi

609 (p=0.0054), 5 dpi (p=0.0257), 6 dpi (p=0.0004), and 8 dpi (p=0.0453). A noticeable trend in

610 severity was also noted on 7 dpi as compared with sham-inoculated controls (p=0.0654). **(B)**

611 Lethargy and increased respiratory effort were the most prominent clinical signs observed in
612 SARS-CoV-2-infected cats; both of which were significantly increased between days 3 and 4
613 (p=0.0027; p=0.0027) and remained significantly elevated in infected cats after 4 dpi as
614 compared to day 0. Coughing was most prominent on 4 dpi and was identified in 4/12 infected
615 cats. Pyrexia was noted in 8/12 cats over the course of the study. Data are expressed as means ±
616 SEM. Statistical comparisons made via mixed effects analysis. *p<0.05; **p<0.01; ***p<0.001;
617 ****p<0.0001.

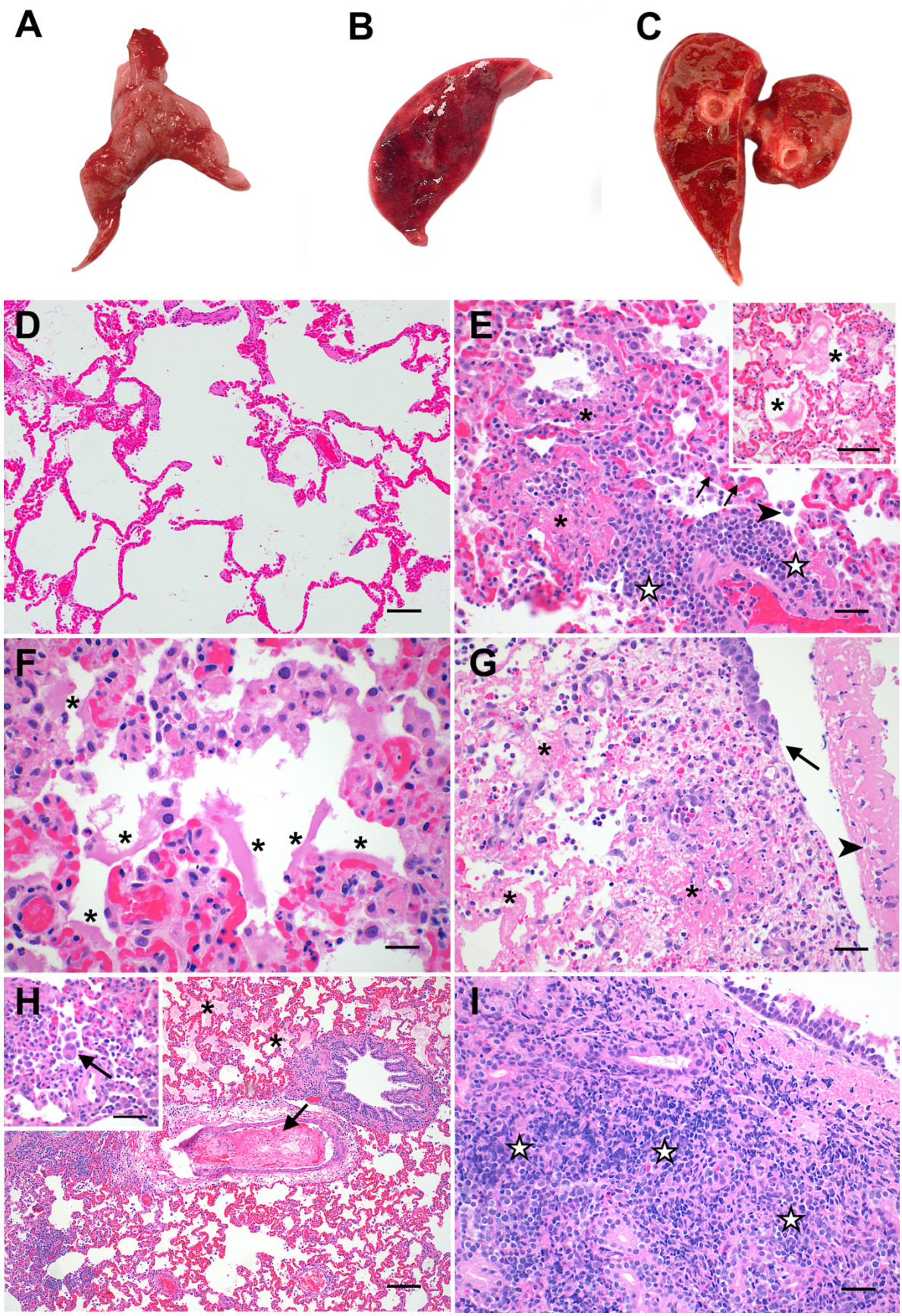

618

619 **Fig 2. Pathologic features of acute SARS-CoV-2 infection in cats are analogous to the**
620 **exudative phase of COVID-19.** Compared to lungs from healthy sham-inoculated cats **(A)**, the
621 lungs of SARS-CoV-2-infected cats were diffusely consolidated, dark red and edematous at both
622 4 dpi **(B)** and 8 dpi **(C)**. The lungs of healthy, uninfected cats **(D)** were histologically normal,
623 with open alveoli and minimal atelectasis. At 4 dpi, the lungs of SARS-CoV-2-infected cats **(E)**
624 exhibited discrete foci of alveolar inflammation and necrosis with fibrin deposition (✱),
625 increased alveolar macrophages (arrowhead), perivascular lymphocytes (☆), and type II
626 pneumocyte hyperplasia (arrows). The alveoli in these cats' lungs were frequently filled with
627 large amounts of edema and fibrin strands **(E** inset**)**, and there were multifocal areas of hyaline
628 membrane formation **(F)** (✱). The distal trachea of 1 SARS-CoV-2 infected cat **(G)** was
629 multifocally ulcerated at 4 dpi (arrow) with diphtheritic membrane formation (arrowhead) and
630 multifocal areas of submucosal necrosis and fibrinoid vasculitis (✱). At 8 dpi **(H)**, fibrinoid
631 vasculitis, vascular thrombosis (arrow), and occasional syncytial cells **(H** inset**)** were observed in
632 addition to the histopathologic changes described above. Tracheal lesions observed at 8 dpi **(I)**
633 were characterized by varying degrees of lymphoplasmacytic, histiocytic, and neutrophilic
634 inflammation with multifocal areas of submucosal necrosis. Magnification: (D, H) 10x, scale bar
635 = 100µm; (E) 20x, scale bar = 50µm; (E inset, G, H inset, I) 40x, scale bar = 25µm; (F) 60x,
636 scale bar = 17µm

637 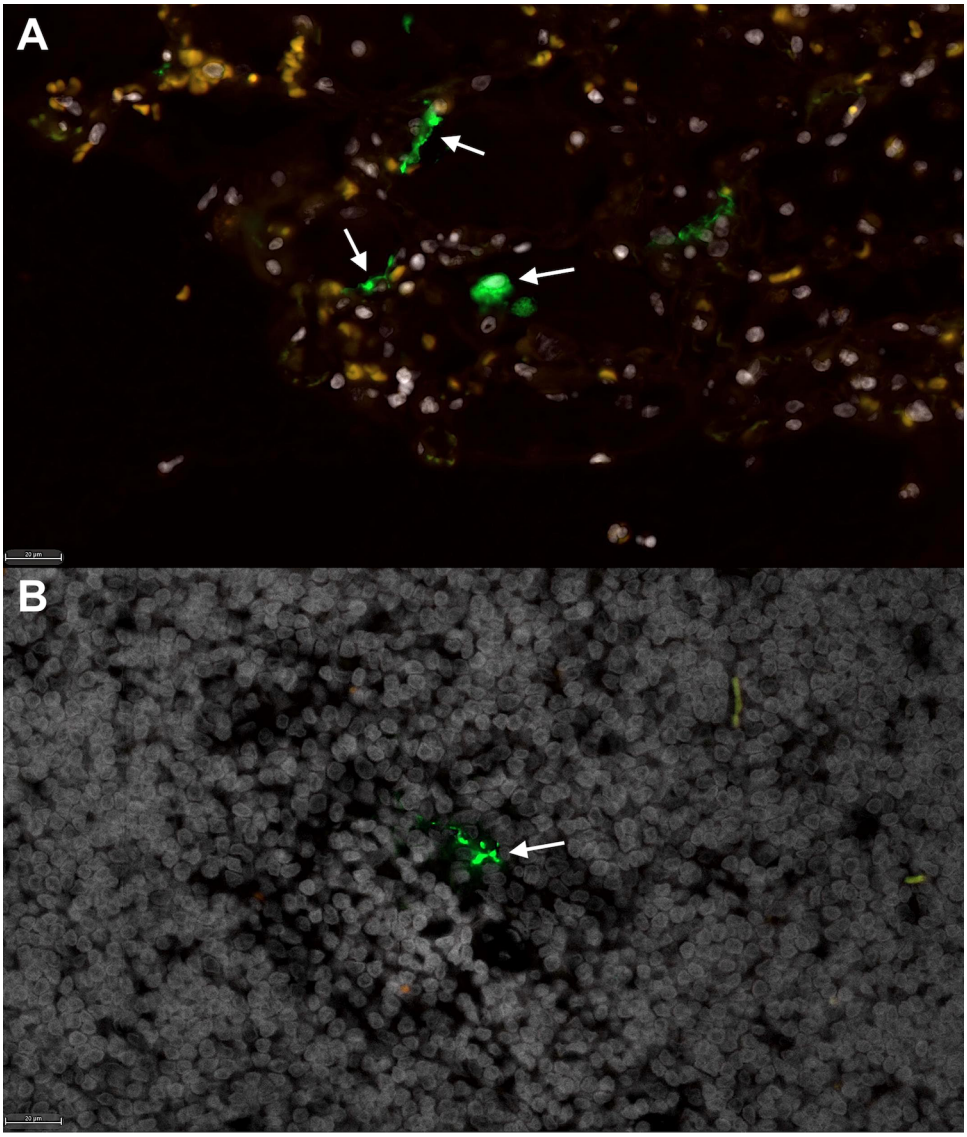

638 **Fig 3. Fluorescent immunohistochemistry for SARS-CoV-2 nucleoprotein identifies**
639 **mononuclear cells in tracheobronchial lymph node of intratracheally-infected cats.** Low
640 numbers of SARS-CoV-2 positive cells (green, white arrows) are detected in **(A)** positive control
641 tissue (lung) from an African Green Monkey infected with SARS-CoV-2 (51), and within **(B)**
642 mononuclear cells in the TB LN of SARS-CoV-2 infected cats (green, white arrow). White =
643 DAPI/nuclei; green = CoV-2. Magnification (A-B) 40x, scale bar = 20 µm.

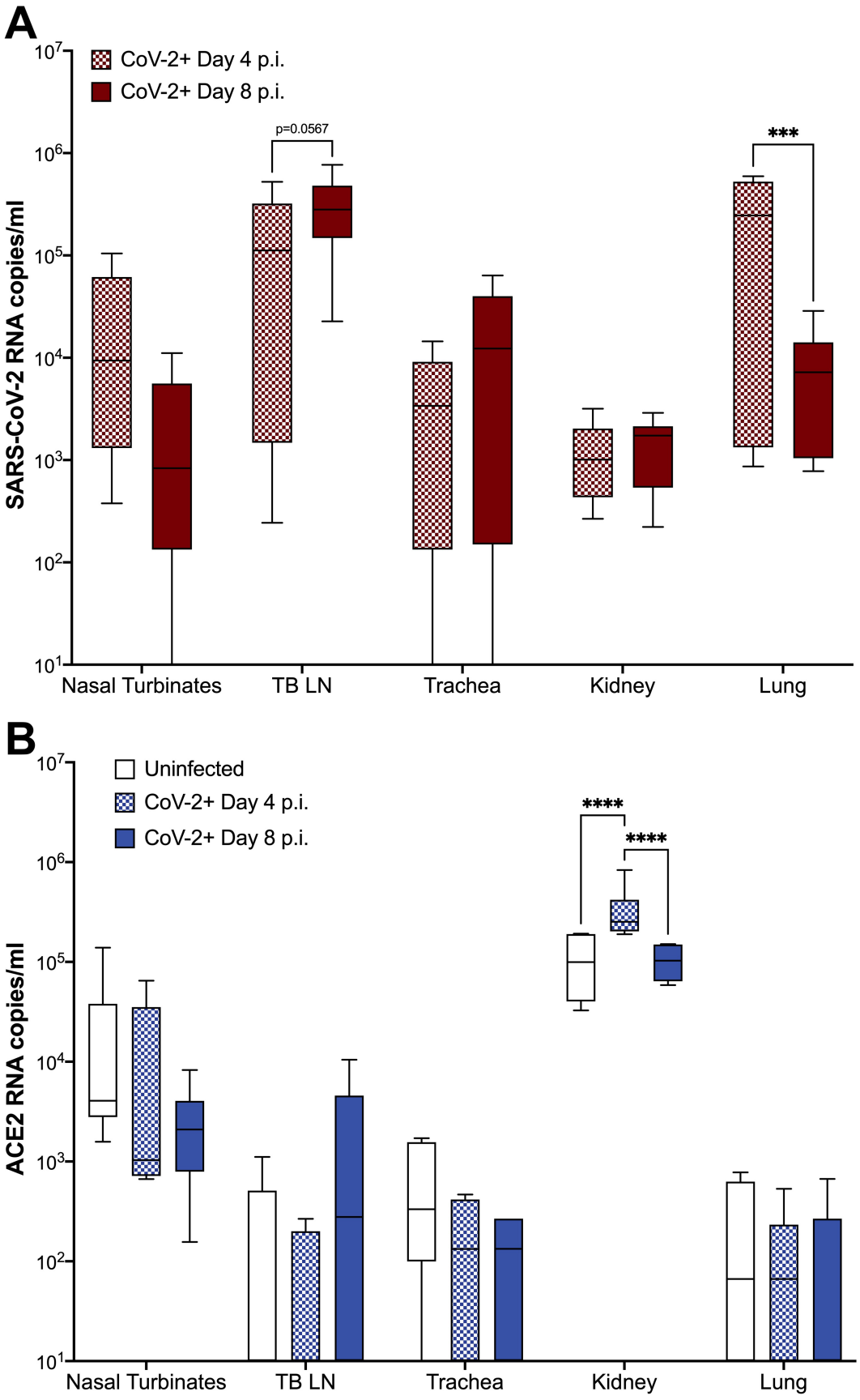
A
CoV-2+ Day 4 p.i.
CoV-2+ Day 8 p.i.
p=0.0567
***
SARS-CoV-2 RNA copies/ml
10^7
10^6
10^5
10^4
10^3
10^2
10^1
Nasal Turbinates
TB LN
Trachea
Kidney
Lung
B
Uninfected
CoV-2+ Day 4 p.i.
CoV-2+ Day 8 p.i.
****
****
ACE2 RNA copies/ml
10^7
10^6
10^5
10^4
10^3
10^2
10^1
Nasal Turbinates
TB LN
Trachea
Kidney
Lung

644

645 **Fig 4. fACE2 RNA and SARS-CoV-2 viral RNA quantification in feline tissues.** Extraction
646 of SARS-CoV-2 and ACE2 RNA was performed as described from tissues samples collected on
647 either 4 or 8 dpi. Tissue samples included nasal turbinates, tracheobronchial lymph node (TB
648 LN), trachea, kidney, and lung. **(A)** SARS-CoV-2 RNA copies were detected in all tissues
649 collected from cats inoculated with SARS-CoV-2. No viral RNA was detected in tissues from
650 sham-inoculated cats. In SARS-CoV-2-infected cats, viral RNA copies were slightly increased in
651 the TB LN between 4 to 8 dpi (p=0.0567) while viral RNA load in the lungs significantly
652 decreased over the same period (p=0.0007). **(B)** fACE2 receptor RNA is significantly increased
653 in the kidney of SARS-CoV-2 infected cats at 4 dpi compared to sham-inoculated controls
654 (p<0.0001) SARS-CoV-3-infected cats at 8 dpi (p<0.0001). Data are expressed as means ± SEM.
655 n=6 cats per group. Statistical comparisons made via two-way ANOVA. ***p<0.001;
656 ****p<0.0001.

657

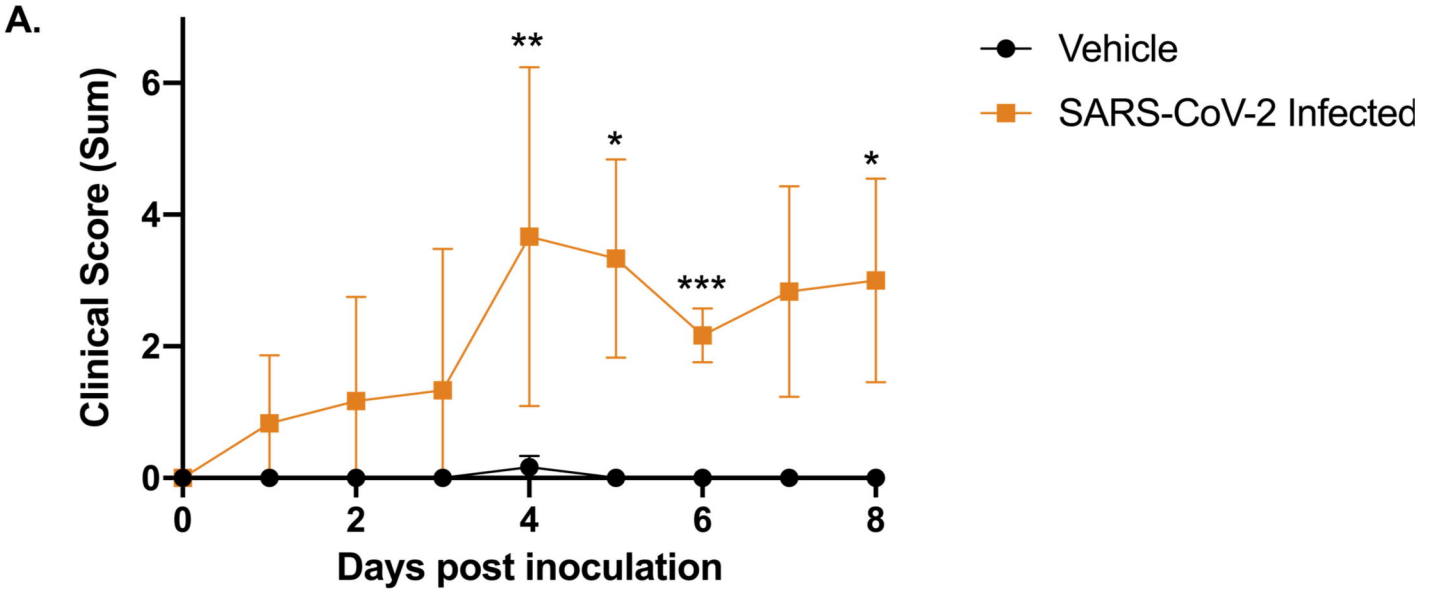
A.
Clinical Score (Sum)
Days post inoculation
Vehicle
SARS-CoV-2 Infected
**
*
***
*
0
2
4
6
8

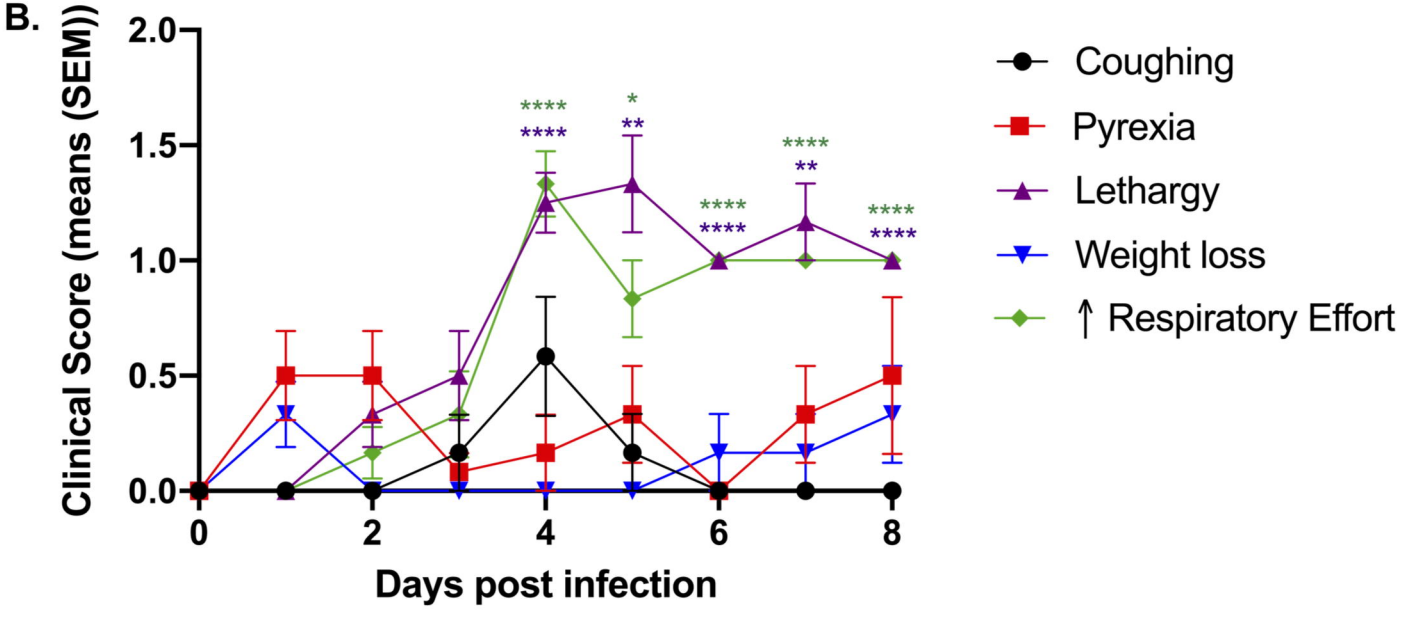
B.
Clinical Score (means (SEM))
Days post infection
Coughing
Pyrexia
Lethargy
Weight loss
↑ Respiratory Effort
2.0
1.5
1.0
0.5
0.0
0
2
4
6
8

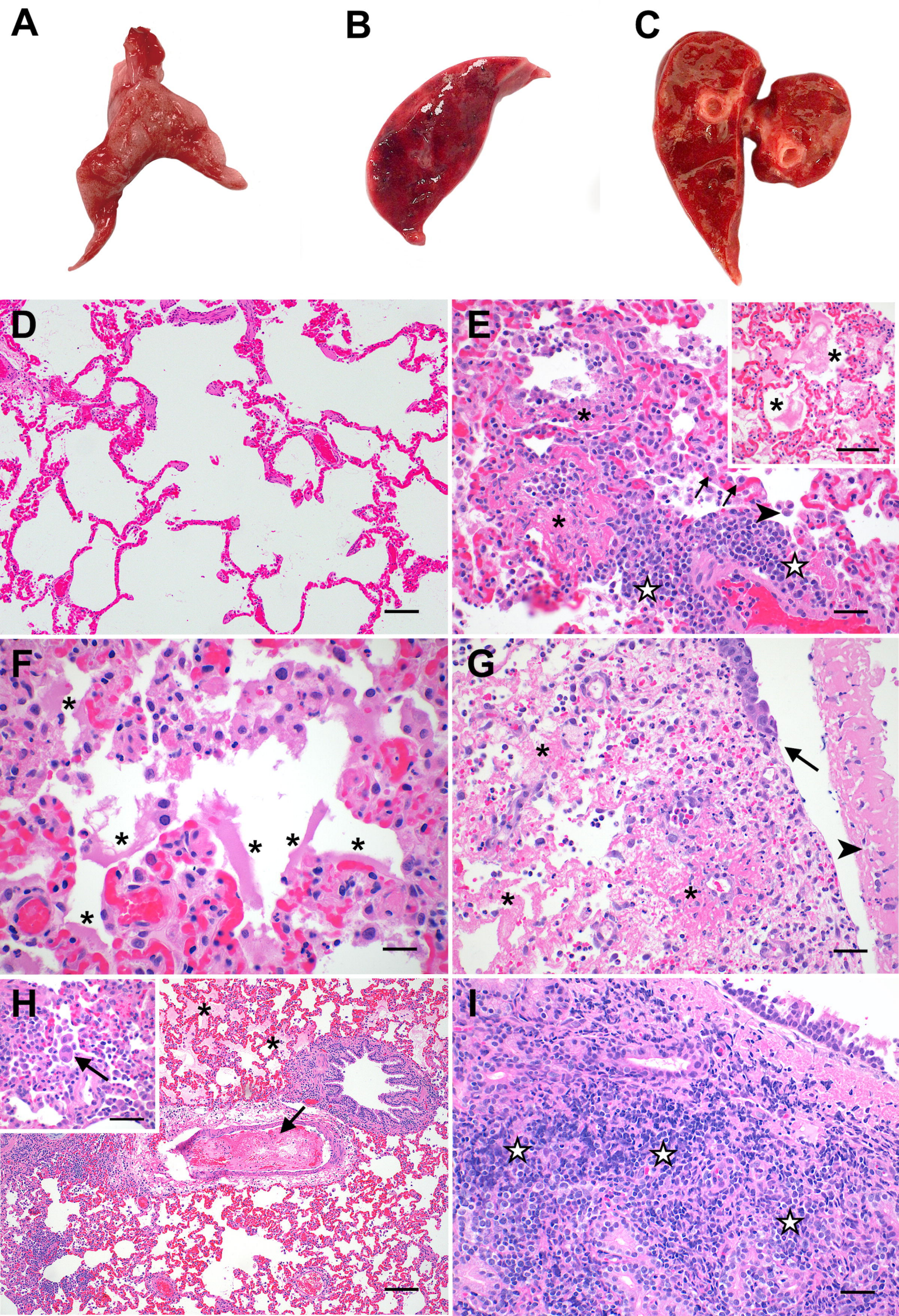
A
B
C
D
E
F
G
H
I

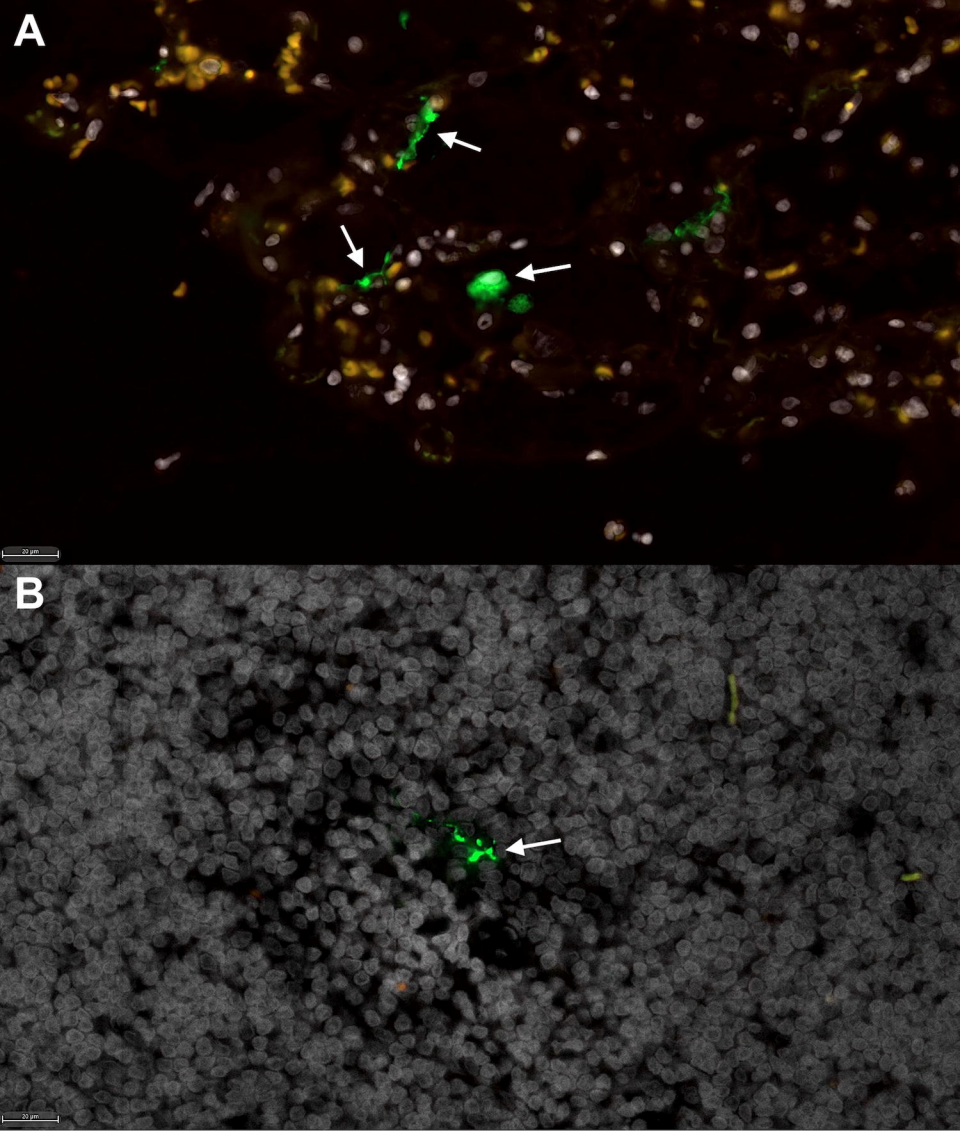
A
20 µm
B
20 µm

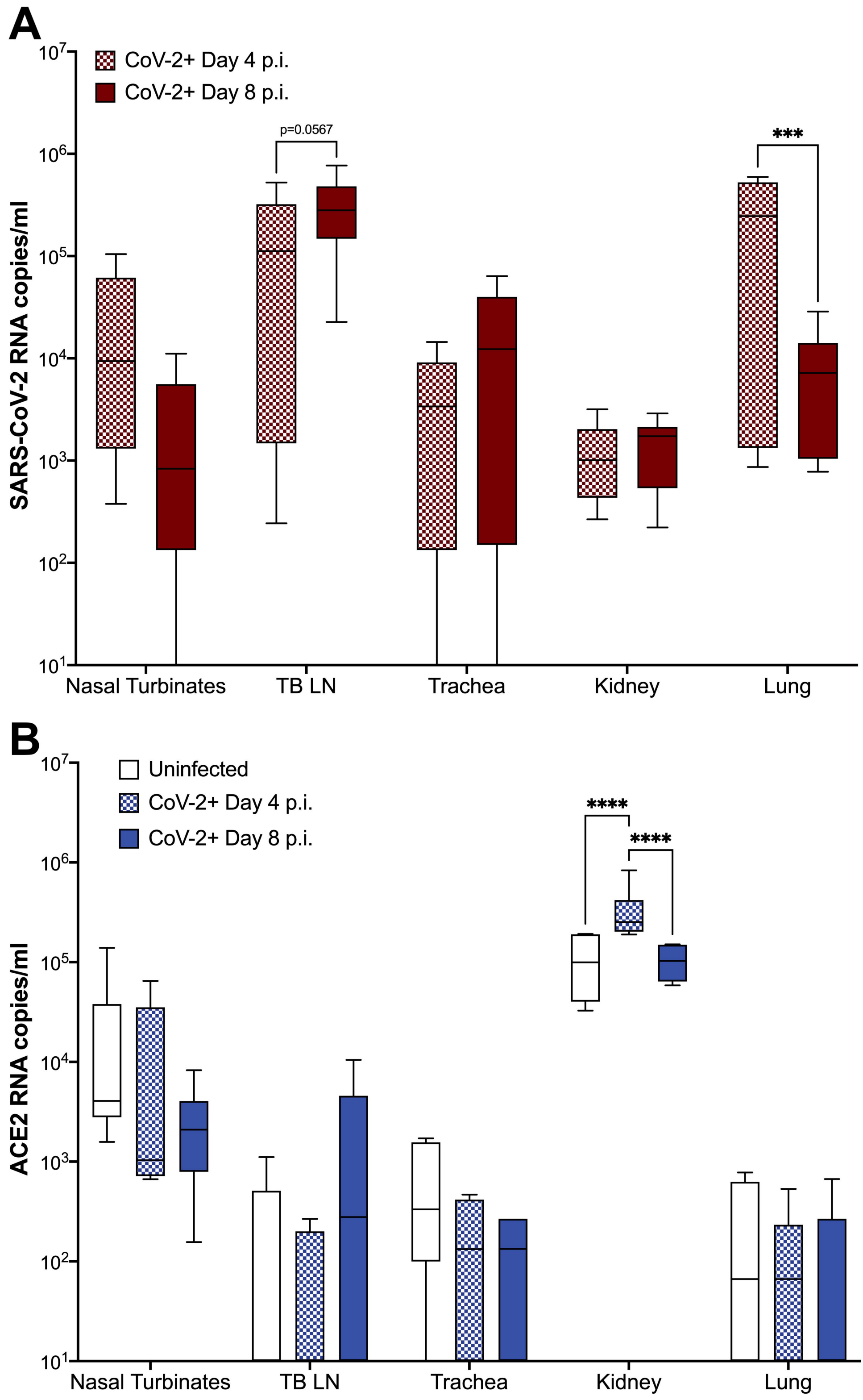
A
CoV-2+ Day 4 p.i.
CoV-2+ Day 8 p.i.
SARS-CoV-2 RNA copies/ml
10^7
10^6
10^5
10^4
10^3
10^2
10^1
p=0.0567
***
Nasal Turbinates
TB LN
Trachea
Kidney
Lung
B
Uninfected
CoV-2+ Day 4 p.i.
CoV-2+ Day 8 p.i.
ACE2 RNA copies/ml
10^7
10^6
10^5
10^4
10^3
10^2
10^1
****
****
Nasal Turbinates
TB LN
Trachea
Kidney
Lung